WILEY-VCH

Unraveling the rate-dependent stability of metal anodes and its implication in designing cycling protocol

*Zhen Hou, Yao Gao, Rui Zhou, Biao Zhang**

Z. Hou, Dr. Y. Gao, R. Zhou, Prof. B. Zhang
Department of Applied Physics, The Hong Kong Polytechnic University, Hung Hom, Hong Kong, China.
E-mail: biao.ap.zhang@polyu.edu.hk

Keywords: Li/K/Zn metal anodes, current rate, Sand's time, nucleation rate, kinetics, thermodynamics, discharge/charge protocol

It is widely recognized that a high current rate (J) speeds up dendrite formation and thus shortens the cycle life of metal anodes. Here, we report an anomalous correlation between elevated J and deposition/stripping stability (decrease-increase-decrease), leading to the relative maximum stability at a moderate J. Complementary theoretical and experimental analyses suggest such a complex relationship lies in high J's dual and contradictory roles in kinetics and thermodynamics. The well-known former renders decreased Sand's time (τ) and deteriorative cyclic stability, while the commonly overlooked latter provides larger extra energy that accelerates nucleation rate (ν_n). Using Zn metal anode as a model system, we unambiguously reveal the ν_n and τ controlled nucleation-growth process, both of which are closely related to J. Based on these findings, we develop an initial high J discharge strategy to produce abundant nuclei for uniform metal growth at standard J in the subsequent process. The protocol increases the Zn deposition/stripping lifetime from 303 h to 2500 h under a cycling capacity of 1 mAh/cm^2 without resorting to electrode/electrolyte modification. Furthermore, such a concept could be readily extended to Li/K metal anodes with significantly enhanced cycle life, demonstrating its universality for developing high-performance metal batteries.

1. Introduction

The fast-growing demand for energy storage technologies in portable electronic devices, electric vehicles, and other electric sectors has aroused a surging interest in seeking reliable and high-energy battery systems.[1-2] Due to the high theoretical capacity and low redox potential, metal anodes, such as Li, K, and Zn, are regarded as promising candidates for next-generation rechargeable batteries.[3-7] However, practical application of these metal anodes is impeded by the dendrite formation during the plating/stripping process.[8-12] As-formed dendrites would facilitate the consumption of limited electrolyte and active anode, resulting in degraded performance and a short lifetime.[13-16] Moreover, the dendrites with sharp tips could easily pierce the separator and cause a short circuit.[17-22]

To reveal the dendrite formation mechanism, several models have been proposed based on complementary theoretical and experimental results.[23-26] Among them, a space-charge model developed by Chazalviel has been widely accepted to elucidate the dendrite initiation.[23] It is found that the dendrite appears when the cation concentration drops to zero in the vicinity of the electrode at a particular time, which is called Sand's time (τ).[27,28] The τ is inversely proportional to J^2 ($\boldsymbol{\tau \propto \frac{1}{J^2}}$). Here J is applied current densities (or current rates in batteries). The equation shows that higher J decreases τ, thus promoting the dendrite growth and causing poor cycle life, which has been widely observed in previous studies.[19,29-32] However, recent research on Li/K metal anodes observe a distinct regime for dendrite evolution at high J (> 9 and 1.5 mA/cm^2 respectively for Li and K), which leads to smoother metal deposition and improved cycle performance compared with the lower one.[33,34] Enhanced cycle performance under high J is also reported in Zn metal anodes most recently.[35] The beneficial role of J may root in the increased nucleation sites, as demonstrated in the early work by Cui's group.[36] These observations indicate the effect of J on the stability of metal electrodes is not straightforward, but a systematic study has lacked with the underlying mechanism elusive.

To unravel the current rate (J) dependent stability of metal electrodes, we adopt Zn metal anode in the aqueous electrolyte as a model system firstly in this study to avoid the potential interference from solid electrolyte interphases (SEIs). It shows that neither high (up to 30 mA/cm^2) nor low J (down to 0.04 mA/cm^2) benefits the cycle life. Instead, a medium J of 5 mA/cm^2 gives rise to the best cyclic stability of 1600 h. We reveal that this surprising plating/stripping stability at moderate J is originated from the double-edged J (adverse kinetic and beneficial thermodynamic characteristics). On the one hand, the high J reduces τ ($\boldsymbol{\tau \propto \frac{1}{J^2}}$) because of rapid electrode surface ion depletion, which deteriorates the cyclic stability. On the

other hand, high J implies a fast nucleation rate (ν_n, $\mathbf{\nu_n \propto exp(-\frac{1}{Log^2 J})}$). This would help to realize uniform Zn deposition at the initial stage. Based on these discoveries, an initial high J (IHJ) cycling protocol is proposed to increase nucleation sites and suppress dendrite growth. As a result, Zn metal anodes could stably run for 2500 h with IHJ (compared to 303 h without IHJ) at 1 mA/cm^2 for 1 mAh/cm^2. Furthermore, this strategy is readily extended to Li/Na/K metal anodes for realizing stable Li/Na/K plating/stripping.

2. Results and discussion

2.1. Anomalously pattern between Zn deposition/stripping lifetime and J

To figure out the relationship between lifetime and J, we systematically collect Zn deposition/stripping performance over a wide J range from 0.04 to 30 mA/cm^2 under three cycling capacities (1, 3 and 5 mAh/cm^2). Lifetime refers to the stable operation time during metal anode deposition/stripping process in the symmetric cells.[37-39] The electrolyte is 2 M $ZnSO_4$ without any modification unless otherwise stated. The detailed voltage versus time profiles is displayed in Figure S1-S3. Surprisingly, lifetime shows a similar but unusual trend with rising J under all tested cycling capacities. The statistical graphs (**Figure 1**a, b and Figure S4) show the cycle life decreases first and then increases to the largest value when the J value climbs. Further increase in the J results in the rapid reduction of the lifespan. Taking the cell with a cycling capacity of 1 mAh/cm^2 as an example, deteriorative stability is observed over two J ranges (from 0.04 to 0.2 mA/cm^2 and between 5 and 30 mA/cm^2). By contrast, improved stability is realized as J rises from 0.2 to 5 mA/cm^2. Consequently, an optimal lifetime of 1600 h at 5 mA/cm^2 is observed. Furthermore, we examine the cycle life in Cu/Zn cells by using Cu foil as the working electrode to better reflect the initial Zn deposition effect (Figure S5 and S6), which indicates the alike J-lifetime relationship as that in Zn/Zn cells. A similar correlation is also observed after changing the electrolyte from 2 M $Zn(SO_4)_2$ to 2 M $Zn(ClO_4)_2$ in Zn/Zn cells (Figure S7 and S8). These results demonstrate the universality of this phenomenon in Zn metal anodes. Such a complex correlation has never been fully revealed.

2.2. Theoretical kinetic and thermodynamic roles of J

To elucidate the underlying science behind this distinct trend, we theoretically evaluate the impact of J. From kinetic considerations, it is well known that τ is dependent on J by the following equation 1[40]:

$$\tau = \pi D \left(\frac{Z_c e C_o}{2 J t_a}\right)^2 \quad \text{(Equation 1)}$$

where τ is the Sand's time (i.e., time of dendrites initiation), D is the diffusion coefficient, Z_c is the cationic charge number, e is the electronic charge, C_0 is the bulk electrolyte concentration,

t_a represents the anionic transference number. In our battery system, this equation could be simplified into $\tau \propto \frac{1}{J^2}$ because other parameters are irrelevant to J. Therefore, higher J renders short τ (Figure 1d), prompting dendrite growth and cell deterioration. This represents J's kinetic characteristic determining the cycle life of Zn metal anodes.

Thermodynamics is the other critical factor for controlling dendrite formation.[41] Gibbs free energy for nucleation could be calculated by summing its bulk free energy and surface free energy (see the Experimental Section).[25] According to classical nucleation theory, nucleation rate (ν_n) and critical radius (r_c) to form a thermodynamically stable nucleus are related to overpotential (η) as follows[42]:

$$\nu_n \propto \exp(-\frac{1}{\eta^2}) \quad \text{(Equation 2)}$$

$$r_c \propto \frac{1}{|\eta|} \quad \text{(Equation 3)}$$

Then, we obtain the relationship between η and J through testing rate performance of Zn/Zn cells (Figure S9). It is shown that $\eta \propto \log J$ (Figure 1c), which agrees well with Butler-Volmer derivation.[43] Thus, equations 2 and 3 can be expressed as follows:

$$\nu_n \propto \exp(-\frac{1}{\mathrm{Log}^2 J}) \quad \text{(Equation 4)}$$

$$r_c \propto \frac{1}{|\mathrm{Log}J|} \quad \text{(Equation 5)}$$

Therefore, large J would increase the ν_n to initiate abundant nuclei with small size (reduced r_c) (Figure 1d and Figure S10).[36,44] This effect could also be explained from the energy barrier point of view. Notably, the nucleation phenomenon is not a spontaneous process, and additional energy is required to overcome the barrier.[45] Low J means a small applied extra energy, so nuclei are preferentially formed at a few sites with low energy barriers, such as crystalline defects and grain boundaries.[3,46] On the contrary, extra energy at higher J enables nuclei at high energy barrier positions, increasing the nucleation seeds. It is well recognized that ample nuclei could suppress dendrite growth and stabilize Zn metal anodes. Therefore, we conjecture that high J should be a double-edged sword according to the above theoretical analysis. It renders short τ from the kinetic side, leading to an unfavorable effect on stability, as widely accepted in the community. Nevertheless, the large J could boost nucleus density from the thermodynamic standpoint and provide a critical yet commonly overlooked role for regulating uniform Zn deposition. The competing roles of J result in the relative maximum stability at a moderate J, which balances the nucleation rates and dendrite growth.

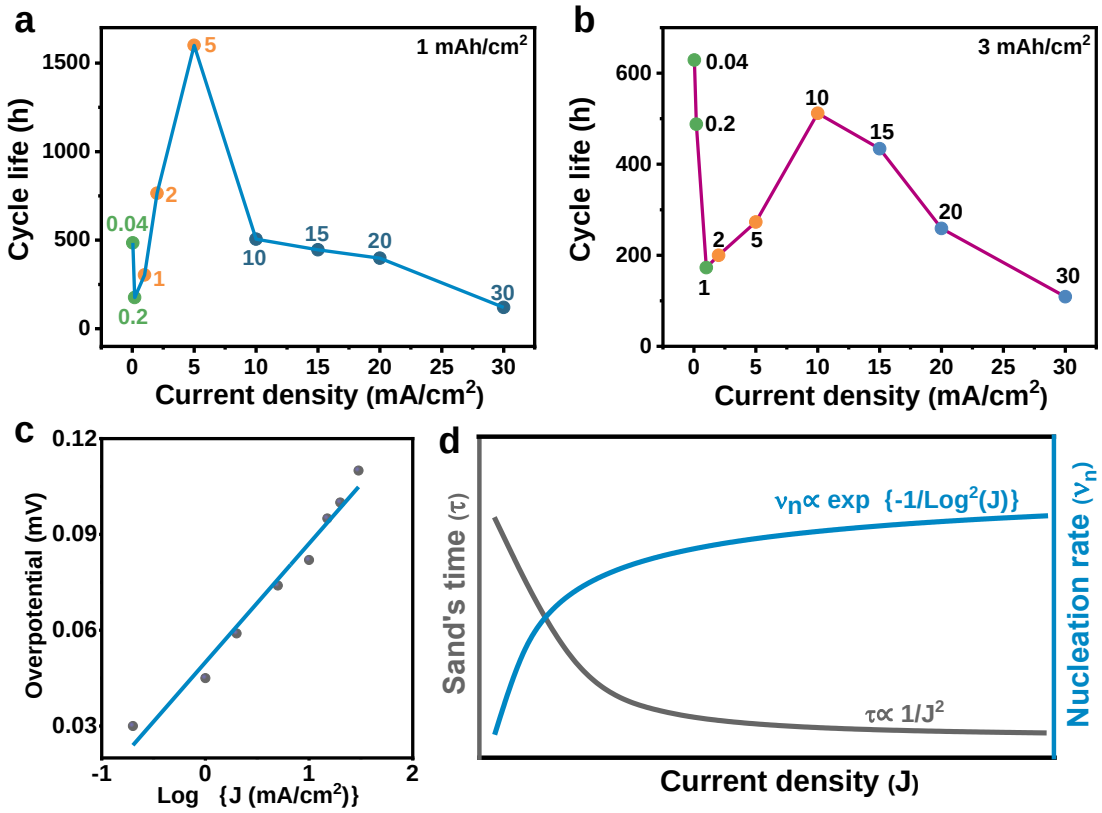

Figure 1. Zn deposition/stripping behavior versus J and the underlying mechanism. Statistical graphs of cycle life versus J of Zn/Zn cells under cycling capacities of a) 1 mAh/cm^2 and b) 3 mAh/cm^2. c) The proportional relationship between overpotential and Log J based on the rate performance result of Zn/Zn cell in Figure S9. d) Theoretical correlation between τ/ν_n and J.

2.3. Experimental verification of underlying mechanism

According to the classic nucleation theory, there are two nucleation mechanisms, i.e., instantaneous and progressive.[47,48] The instantaneous model indicates all nucleation sites are simultaneously activated at the initial deposition process. Zn ions are then deposited on these nuclei in the following growth. In contrast, the progressive model suggests that new nuclei are continuously formed accompanying the Zn growth. Nucleation overpotentials are obtained at both Cu and Zn electrodes to evaluate the Zn nucleation process. As shown in **Figure 2**a and Figure S11, an initial voltage tip (corresponding to nucleation) and a subsequent voltage plateau (corresponding to growth) are observed regardless of the substrates at all the tested J. This indicates the nucleation model should be instantaneous instead of progressive.[36] Furthermore, the chronoamperometry (CA) test is carried out to obtain current-time curves under various overpotentials (Figure S12), which is then analyzed by the Scharifker and Hills (SH) model to precisely distinguish nucleation mechanism.[49] Based on this model, instantaneous nucleation (equation 6) and progressive nucleation (equation 7) are respectively described by:

$$\frac{J^2}{J_{max}^2} = 1.9542\left(\frac{t_{max}}{t}\right)\left[1-\exp\left(-1.2564\frac{t}{t_{max}}\right)\right]^2 \quad \text{Equation (6)}$$

$$\frac{J^2}{J_{max}^2} = 1.2254\left(\frac{t_{max}}{t}\right)\left[1-\exp\left(-2.3367\frac{t^2}{t_{max}^2}\right)\right]^2 \quad \text{Equation (7)}$$

where J_{max} represents maximum current density during the CA test and t_{max} is the corresponding time. The above theoretical curves for 3D instantaneous and progressive nucleation are plotted and compared with the experimental current–time transients (Figure 2b and Figure S13). The experimental Zn nucleation process is relatively close to theoretical response for 3D instantaneous nucleation at all measured overpotentials, which agrees with nucleation overpotential results and previous studies in conventional Zn electrodeposition.[50,51] The deviation of experimental value from perfect instantaneous model prediction is probably originated from hydrogen evolution reaction (HER) during Zn deposition,[52,53] which would provide an additional cathodic current. The presence of HER is confirmed by examining the Zn electrode after cycling (see Figure S14 for details). Therefore, Zn nuclei, which are only generated at the initial deposition process, would significantly influence the subsequent deposition morphologies.

To corroborate the proposed hypothesis for correlation between ν_n and J, we compare the nucleation morphologies under low (0.2 mA/cm^2) and high (5 mA/cm^2) current rates. A small amount of Zn (0.05 mAh/cm^2) is deposited on a highly oriented pyrolytic graphite (HOPG) electrode for clear visualization under an atomic force microscope (AFM). Sparse and large nuclei are observed in low J (Figure 2c), while plenty of small Zn particles are presented when a high J is applied (Figure 2d). The results support well the theoretical predictions where large J promotes the formation of dense Zn nuclei. A systematic study on Cu and Zn electrodes under a wide J range is conducted to explore the substrate effect (Figure S15 and S16). Again, the number of Zn nuclei increases, and their size becomes smaller on both Cu and Zn electrodes as J rises, proving this behavior is independent of substrate materials. For example, a nearly bare electrode surface is found at 0.04 mA/cm^2 on the Cu electrode due to scattered and huge Zn nuclei. With the same deposition amount, the electrode surface is entirely covered by tiny Zn nuclei under 5 mA/cm^2, confirming uniform nucleation could be achieved at higher J.

To assess the effect of J for subsequent Zn growth, which is mainly determined by the kinetics-related Sand's time (τ), the deposition capacity is increased to 1 mAh/cm^2 on both Cu and Zn electrodes. We observe that a large proportion of Cu electrodes is still bare at 0.04 mA/cm^2 (Figure S17). According to the instantaneous nucleation model confirmed before, Zn metal is preferentially deposited on the rare initial Zn nuclei, forming protrusions with a rough surface. On the contrary, a smooth and uniform Zn metal layer is achieved at 5 mA/cm^2,

ascribed to the rich nucleation seeds that guide subsequent Zn deposition. Nevertheless, the surface structure is degraded when the J reaches 20 mA/cm^2. The large J leads to a short τ, which is the main reason for the deterioration at 20 mA/cm^2 despite increased nucleation sites. The comparable phenomenon is also detected on the Zn electrode in Zn/Zn cells (Figure S18). Thus, the deposition behavior is highly coupled to the theoretical prediction, where a medium J gives the most extended cycle life.

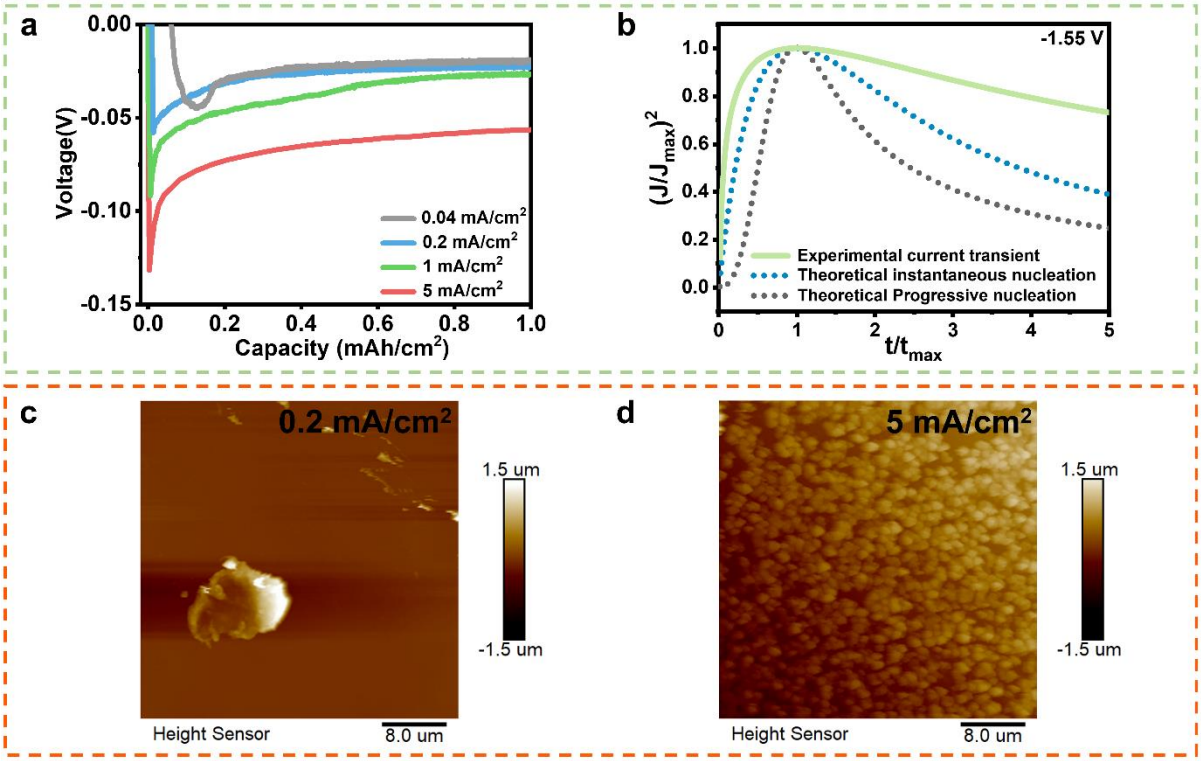

Figure 2. Instantaneous nucleation pattern and experimental correlation between v_n and J. a) Nucleation overpotentials of Cu/Zn cells at various J. b) Non-dimensional plots of experimental current–time transients with theoretical curves for 3D instantaneous and progressive nucleation. AFM images of Zn nucleation on HOPG electrode (0.05 mAh/cm^2) at c) 0.2 mA/cm^2 and d) 5 mA/cm^2.

2.4. Developing an IHJ concept to improve the stability of Zn metal anodes.

Knowing that uniform Zn nuclei could be realized at higher J, we move forward to propose a well-designed discharge/charge protocol for elongating cycle life. Concretely, a short burst at high J is applied at the initial deposition process for generating ample nuclei. Afterward, the cells return to operation at standard (low) J. To demonstrate the effectiveness of initial high J (IHJ) approach, cycle life is tested and compared in both Zn/Zn and Cu/Zn cells without and with IHJ. As shown in Figure S20, at 0.04 mA/cm^2 for 1 mAh/cm^2, cell without IHJ suffers from a short circuit after ~480 h, which should be ascribed to uneven deposition induced by

rare nuclei. When two similar IHJ patterns (5 mA/cm^2 and 10 mA/cm^2 for 0.05 mAh/cm^2) are employed in the cells, the stability is dramatically increased to 2400 h, verifying the superiority of this protocol. We further test cells at higher standard J of 0.2 and 1 mA/cm^2 under the same cycling capacity of 1 mAh/cm^2 (Figure S21 and S22 and **Figure 3**a). Delightedly, highly improved performance is still achieved with IHJ. For example, it is found that IHJ (5 mA/cm^2 for 0.05 mAh/cm^2) approach enables ultra-stable operation for 2500 h at 1 mA/cm^2, which is much better than ~300 h without IHJ. It is noteworthy that such remarkable enhancements surpass the performance of most previous reports,[54] indicating the excellent availability of IHJ method. In addition, similar improvements persist with IHJ at a higher cycling capacity of 3 mAh/cm^2 (Figure S23). Furthermore, this approach is suitable for Cu/Zn cells and Zn/AC full cells (Figure S24 and S25), manifesting its universality and considerable potential for practical application. Combining the optimal cycling current density and IHJ protocol could further extend our findings to other application scenarios, such as Zn/$Zn_xV_2O_5{\cdot}H_2O$ full cells (see Figure S26 and S27 for details). The working mechanism of IHJ should be as follows: the abundant nuclei formed at high J help regulate subsequent deposition at standard J, generating a smooth Zn metal layer. This is confirmed by SEM images without/with IHJ (Figure S28 and Figure 3b and c). Nonuniform and porous Zn bulges are detected on the deposition layer without IHJ at both 0.04 and 1 mA/cm^2, while flat and dense Zn deposition is observed with IHJ.

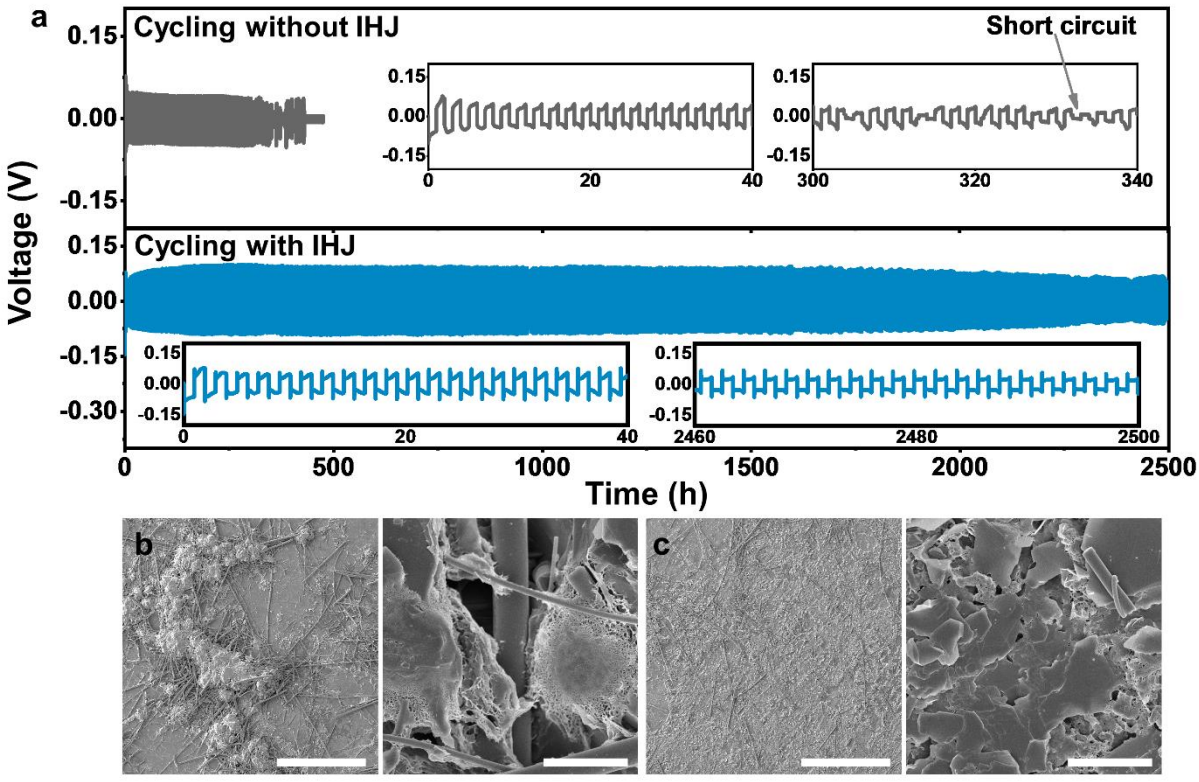

Figure 3. An IHJ approach for prolonged cycle performance. a) The cycle performance of Zn/Zn cells without and with IHJ (5 mA/cm^2 for 0.05 mAh/cm^2) at 1 mA/cm^2 for 1 mAh/cm^2 and detailed plating/stripping curves (inset). Morphological characterization of first Zn deposition at 1 mA/cm^2 for 1 mAh/cm^2 on Zn metal anode b) without and c) with IHJ (5 mA/cm^2 for 0.05 mAh/cm^2). The scale bars for the left and right one in each figure are respectively 200 and 5 μm.

2.5. Universality of IHJ approach for Li/Na/K metal anodes

To explore the broader application of our concept, we investigate the deposition behavior of Li/Na/K metal anodes without/with IHJ. These metals are promising anodes for high-energy-density batteries, but they also suffer from the notorious issue of dendrite growth.[5,39,55] AFM images of 1 mAh/cm^2 Li deposition are collected to evaluate the effect of IHJ. The Li deposition is rough and nonuniform at 0.5 mA/cm^2 without IHJ (**Figure 4**a). Its average roughness (R_a) is as high as 745 nm, attributed to deficient Li nuclei (Figure S29b). By contrast, assisted by abundant Li nuclei triggered at the IHJ (5 mA/cm^2 for 0.05 mAh/cm^2) (Figure S29c), the morphology becomes smoother and more uniform (Figure 4b): R_a value decreases to 479 nm. Thus, it is expected that an enhanced lifetime could be realized with IHJ. As shown in Figure 4c and Figure S30, in contrast to short circuit that occurred in Li metal anodes after 790 h in the absence of IHJ at 0.5 mA/cm^2 for 1 mAh/cm^2, cells could stably run for 2100 h with two similar IHJ (5 mA/cm^2 and 8 mA/cm^2 for 0.05 mAh/cm^2) in the same testing condition. Pushing to a higher standard J of 1 mA/cm^2, IHJ still provides a three-fold improvement for plating/stripping lifetime (Figure S31). IHJ approach could also benefit the Na and K metal anodes (Figure S32 and Figure 4d). Specifically, a stable Na deposition/stripping process with much smoother voltage profiles could be realized in the presence of IHJ. Turning to the K metal anodes, IHJ (1 mA/cm^2 for 0.05 mAh/cm^2) could increase the stability from ~270 h to 1300 h at 0.25 mA/cm^2 for 1 mAh/cm^2 using highly corrosive carbonate electrolyte. According to the previous studies, the self-heating-induced healing of Li and K dendrites would be triggered when current densities are higher than 8 and 1.5 mA/cm^2, respectively.[33,34] Thus, to avoid the potential interference of self-healing, the employed current densities at the IHJ process for Li/K anodes are lower than these values. Besides, such phenomenon is not reported on Zn anode due possibly to the high melting point of Zn. Noteworthily, the performance of our approach for Li/K metal anodes is comparable to previous works[56-58] without resorting to electrolyte and electrode modification. In short, the IHJ approach could be easily applied to Li/Na/K metal anodes.

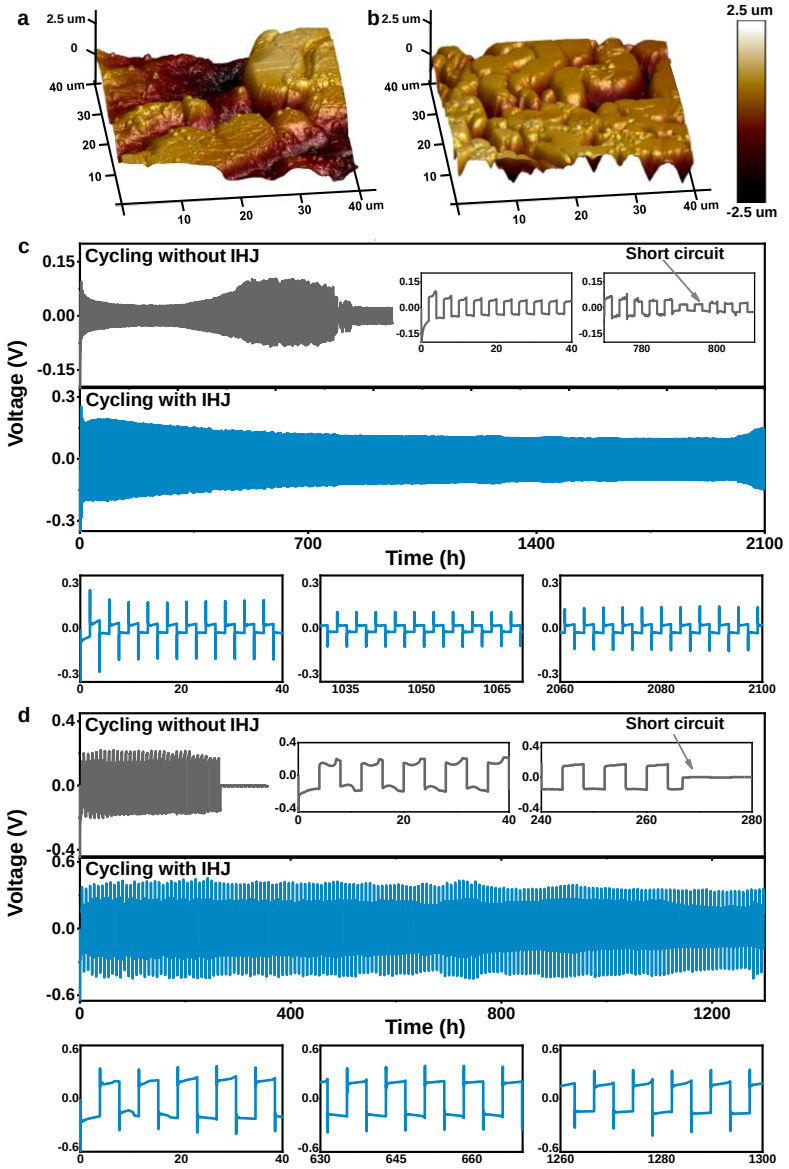

Figure 4. Improved electrochemical performance of Li/K metal anodes with IHJ. AFM images of Li deposition (1 mAh/cm^2) on Li electrode a) without and b) with IHJ (5 mA/cm^2 for 0.05 mAh/cm^2) at 0.5 mA/cm^2. c) The cycle performance of Li/Li cells without and with IHJ (5 mA/cm^2 for 0.05 mAh/cm^2) at 0.5 mA/cm^2 for 1 mAh/cm^2 and detailed plating/stripping curves of certain cycles. d) The cycle performance of K/K cells without and with IHJ (1 mA/cm^2 for 0.05 mAh/cm^2) at 0.25 mA/cm^2 for 1 mAh/cm^2 and detailed plating/stripping curves of certain cycles.

3. Conclusion

We explore the double-edged effects of J on cyclic stability through complementary theoretical analysis and experimental investigation. On the one hand, high J brings about instability through decreasing τ based on the well-known kinetic role of J. On the other hand, it could provide large nucleation overpotential and increase nucleation sites from a thermodynamic

point of view according to the experimental observations, contributing to the enhanced stability. Based on these findings, an IHJ concept is developed to form sufficient nuclei at a high J for guiding subsequent Zn deposition at a standard (lower) J. The inclusion of IHJ could effectively improve the cycle life of Zn metal anodes from 303 h to 2500 h. Furthermore, the strategy with broader utility is readily employed in Li (790 h without IHJ and 2100 h with IHJ) and K (270 h without IHJ and 1300 h with IHJ) metal anodes. This work would provide fresh insights into the effect of J on the metal anodes plating/stripping process and boost the development of stable metal batteries by simply manipulating discharge/charge protocols.

4. Experimental Section

Preparation of electrolyte and cathodes: 2 M $ZnSO_4$ (zinc sulfate heptahydrate, Aalfa Aesar, 98%) in pure water was used as electrolyte unless otherwise stated. The modified $Zn_xV_2O_5{\cdot}H_2O$ material was synthesized by a simple hydrothermal method. Detailed synthesis procedure and the structure of cathode are given in the supporting information (Figure 26). The $Zn_xV_2O_5{\cdot}H_2O$ slurry was prepared by uniformly mixing 70 wt% $Zn_xV_2O_5{\cdot}H_2O$ powder, 20 wt% Super P and 10 wt% polyvinylidene fluoride (PVDF) in N-methyl-2-pyrrolidone. The cathodes were fabricated by casting the slurry onto the stainless-steel foils and then dried at 60 °C for 12 h. The activated carbon (AC) slurry consisting of 80 wt% AC and 20 wt% poly(vinylidene fluoride-co-trifluoroethylene) in acetone was poured into a flat watch-glass and dried at 60 °C for 12 h. Finally, free-standing AC cathodes were cut into circular disks with a mass loading of ~18.4 mg/cm^2.

Characterizations: The morphologies of Zn metal anodes were examined by scanning electron microscope (SEM) (TESCAN MAIA3). Atomic force microscope (AFM) test was carried out on the Bruker Dimension Icon AFM. X-ray diffraction (XRD) pattern was acquired using an X-ray diffractometer (Rigaku SmartLab) with Cu Ka radiation. Since aqueous electrolytes are adopted, we disassemble the cells in the air and the cycled Zn electrodes are exposed to the atmosphere. Nonetheless, the morphology change of Zn should be negligible as Zn does not react severely with the air except for slight oxidation (Figure S19).

Electrochemical measurements: CR2032 coin-type cells were assembled using Cu/Zn metal (diameter of 12 mm) and Zn metal (diameter of 12 mm) respectively as the working electrode and counter/reference electrode, with the glass fiber (diameter of 19 mm) as the separators. Each cell contained 100 uL electrolytes. Cu/Zn and Zn/Zn cells were tested at various current densities and cycling capacities. Cu/Zn cells were cycled with a discharge time of 1 h and charge cut-off voltage of 0.5 V at 1 mA/cm^2. CE values were then calculated based on the capacity

ratio of charge to discharge. The electrolytes for Li/Li, Na/Na and K/K cells were 1 M LiTFSI in DOL/DME, 1 M $NaPF_6$ in EC/PC, and 1 M KFSI in EC/DMC, respectively. A three-electrode system (beaker-type with a volume of 50 mL) was used to carry out chronoamperometry (CA) test to analyze the Zn nucleation model. Pt (diameter of 2 mm) was employed as a working electrode, and Zn metal (diameter of 12 mm) and Hg/Hg_2SO_4 were respectively used as counter and reference electrodes. Zn/AC and Zn/ $Zn_xV_2O_5{\cdot}H_2O$ full cells were cycled between 0.2 and 1.8 V and 0.2 and 1.6 V, respectively.

Calculations: For thermodynamic character, Gibbs free energy for nucleation could be calculated by summing its bulk free energy and surface free energy: $\Delta G_n = -\frac{4\pi}{3} r^3 \Delta G_v + 4\pi r^2 \gamma$ (Equation 8), where ΔG_N and ΔG_V are respectively free energy for nucleation and free energy change per volume, γ relates to the surface tension between nuclei and electrolyte. ΔG_V could be further expressed as: $\Delta G_v = -\frac{nF|\eta|}{V_m}$ (Equation 9), where n is the cationic charge number, F is Faraday's constant, η is overpotential, V_m is the molar volume. Then, we can deduce critical radius (r_c) to form a thermodynamically stable nucleus as follows: $r_c = \frac{2\gamma V_m}{nF|\eta|}$ (Equation 10). In addition, nucleation rate (ν_n) could be expressed as: $\nu_n = \exp(-\frac{k}{\eta^2})$ (Equation 11), where k is nucleation constant.

Supporting Information

Supporting Information is available from the Wiley Online Library or from the author.

Acknowledgements

This work was supported by the General Research Fund (GRF) scheme of the Hong Kong Research Grants Council (15301220), and the Hong Kong Polytechnic University (ZVGH and ZVRP, and ZE2F).

Received: ((will be filled in by the editorial staff))

Revised: ((will be filled in by the editorial staff))

Published online: ((will be filled in by the editorial staff))

References

[1] J. M. Tarascon, M. Armand, *Nature* **2001**, *414*, 359.

[2] D. Chao, W. Zhou, F. Xie, C. Ye, H. Li, M. Jaroniec, S. Z. Qiao, *Sci. Adv.* **2020**, *6*, eaba4098.

[3] X. B. Cheng, R. Zhang, C. Z. Zhao, Q. Zhang, *Chem. Rev.* **2017**, *117*, 10403.

[4] W. Xu, J. Wang, F. Ding, X. Chen, E. Nasybulin, Y. Zhang, J.-G. Zhang, *Energy Environ. Sci.* **2014**, *7*, 513.

[5] W. Liu, P. Liu, D. Mitlin, *Adv. Energy Mater.* **2020**, *10*, 2070177.

[6] Q. Zhang, J. Luan, Y. Tang, X. Ji, H. Wang, *Angew. Chem. Int. Ed.* **2020**, *59*, 13180.

[7] T. Zhang, Y. Tang, S. Guo, X. Cao, A. Pan, G. Fang, J. Zhou, S. Liang, *Energy Environ. Sci.* **2020**, *13*, 4625.

[8] D. Lin, Y. Liu, Y. Cui, *Nat. Nanotechnol.* **2017**, *12*, 194.

[9] J. Xiang, L. Yang, L. Yuan, K. Yuan, Y. Zhang, Y. Huang, J. Lin, F. Pan, Y. Huang, *Joule* **2019**, *3*, 2334.

[10] Y. Jie, X. Ren, R. Cao, W. Cai, S. Jiao, *Adv. Funct. Mater.* **2020**, *30*, 1910777.

[11] C. Liu, X. Xie, B. Lu, J. Zhou, S. Liang, *ACS Energy Lett.* **2021**, *6*, 1015.

[12] J. Hao, X. Li, X. Zeng, D. Li, J. Mao, Z. Guo, *Energy Environ. Sci.* **2020**, *13*, 3917.

[13] V. Verma, S. Kumar, W. Manalastas, M. Srinivasan, *ACS Energy Lett.* **2021**, *6*, 1773.

[14] Z. Zhao, J. Zhao, Z. Hu, J. Li, J. Li, Y. Zhang, C. Wang, G. Cui, *Energy Environ. Sci.* **2019**, *12*, 1938.

[15] S. Liu, J. Mao, W. K. Pang, J. Vongsvivut, X. Zeng, L. Thomsen, Y. Wang, J. Liu, D. Li, Z. Guo, *Adv. Funct. Mater.* **2021**, *31*, 2104281

[16] H. Dong, J. Li, J. Guo, F. Lai, F. Zhao, Y. Jiao, D. J. L. Brett, T. Liu, G. He, I. P. Parkin, *Adv. Mater.* **2021**, *33*, e2007548.

[17] X. Li, T. Li, P. Xu, C. Xie, Y. Zhang, X. Li, *Adv. Funct. Mater.* **2021**, *31*, 2100133.

[18] C. Deng, X. Xie, J. Han, Y. Tang, J. Gao, C. Liu, X. Shi, J. Zhou, S. Liang, *Adv. Funct. Mater.* **2020**, *30*, 2000599.

[19] Q. Yang, Q. Li, Z. Liu, D. Wang, Y. Guo, X. Li, Y. Tang, H. Li, B. Dong, C. Zhi, *Adv. Mater.* **2020**, *32*, e2001854.

[20] L. Zhang, B. Zhang, T. Zhang, T. Li, T. Shi, W. Li, T. Shen, X. Huang, J. Xu, X. Zhang, Z. Wang, Y. Hou, *Adv. Funct. Mater.* **2021**, *31*, 2100186.

[21] G. Garcia, E. Ventosa, W. Schuhmann, *ACS Appl. Mater. Interfaces* **2017**, *9*, 18691.

[22] X. Guo, Z. Zhang, J. Li, N. Luo, G.-L. Chai, T. S. Miller, F. Lai, P. Shearing, D. J. L. Brett, D. Han, Z. Weng, G. He, I. P. Parkin, *ACS Energy Lett.* **2021**, *6*, 395.

[23] J. Chazalviel, *Phys. Rev. A* **1990**, *42*, 7355.

[24] J. L. Barton, J. O. M. Bockris, *Proc. R. Soc. Lond., A Math. Phys. Sci.* **1962**, *268*, 485.

[25] D. R. Ely, R. E. García, *J. Electrochem. Soc.* **2013**, *160*, A662.

[26] J. T. Kim, J. Jorné, *J. Electrochem. Soc.* **1980**, *127*, 8.

[27] M. K. Aslam, Y. Niu, T. Hussain, H. Tabassum, W. Tang, M. Xu, R. Ahuja, *Nano Energy* **2021**, *86*, 106142

[28] H. J. S. Sand, *London Edinburgh Philos. Mag. J. Sci.* **2010**, *1*, 45.

[29] P. Shi, X. B. Cheng, T. Li, R. Zhang, H. Liu, C. Yan, X. Q. Zhang, J. Q. Huang, Q. Zhang, *Adv. Mater.* **2019**, *31*, e1902785.

[30] V. Yufit, F. Tariq, D. S. Eastwood, M. Biton, B. Wu, P. D. Lee, N. P. Brandon, *Joule* **2019**, *3*, 485.

[31] Z. Lu, Q. Liang, B. Wang, Y. Tao, Y. Zhao, W. Lv, D. Liu, C. Zhang, Z. Weng, J. Liang, H. Li, Q.-H. Yang, *Adv. Energy Mater.* **2019**, *9*, 1803186.

[32] D. Han, S. Wu, S. Zhang, Y. Deng, C. Cui, L. Zhang, Y. Long, H. Li, Y. Tao, Z. Weng, Q. H. Yang, F. Kang, *Small* **2020**, *16*, e2001736.

[33] L. Li, S. Basu, Y. Wang, Z. Chen, P. Hundekar, B. Wang, J. Shi, Y. Shi, S. Narayanan, N. Koratkar, *Science* **2018**, *359*, 1513.

[34] P. Hundekar, S. Basu, X. Fan, L. Li, A. Yoshimura, T. Gupta, V. Sarbada, A. Lakhnot, R. Jain, S. Narayanan, Y. Shi, C. Wang, N. Koratkar, *Proc. Natl. Acad. Sci. U. S. A.* **2020**, *117*, 5588.

[35] H. Glatz, E. Tervoort, D. Kundu, *ACS Appl. Mater. Interfaces* **2020**, *12*, 3522.

[36] A. Pei, G. Zheng, F. Shi, Y. Li, Y. Cui, *Nano Lett.* **2017**, *17*, 1132.

[37] Y. Lu, Z. Tu, L. A. Archer, *Nat. Mater.* **2014**, *13*, 961.

[38] X. Cao, X. Ren, L. Zou, M. H. Engelhard, W. Huang, H. Wang, B. E. Matthews, H. Lee, C. Niu, B. W. Arey, Y. Cui, C. Wang, J. Xiao, J. Liu, W. Xu, J.-G. Zhang, *Nat. Energy* **2019**, *4*, 796.

[39] J. L. Ma, F. L. Meng, Y. Yu, D. P. Liu, J. M. Yan, Y. Zhang, X. B. Zhang, Q. Jiang, *Nat. Chem.* **2019**, *11*, 64.

[40] M. Rosso, C. Brissot, A. Teyssot, M. Dollé, L. Sannier, J.-M. Tarascon, R. Bouchet, S. Lascaud, *Electrochim. Acta* **2006**, *51*, 5334.

[41] X. Gao, Y.-N. Zhou, D. Han, J. Zhou, D. Zhou, W. Tang, J. B. Goodenough, *Joule* **2020**, *4*, 1864.

[42] W. Plieth, *Electrochemistry for materials science*, Elsevier, **2008**.

[43] V. S. Bagotsky, *Fundamentals of electrochemistry*, John Wiley & Sons, **2005**.

[44] P. Biswal, S. Stalin, A. Kludze, S. Choudhury, L. A. Archer, *Nano Lett.* **2019**, *19*, 8191.

[45] A. Milchev, *Electrocrystallization: fundamentals of nucleation and growth*, Springer Science & Business Media, **2002**.

[46] C. Wang, A. Wang, L. Ren, X. Guan, D. Wang, A. Dong, C. Zhang, G. Li, J. Luo, *Adv. Funct. Mater.* **2019**, *29*, 1905940.

[47] G. Hills, D. Schiffrin, J. Thompson, *Electrochim. Acta* **1974**, *19*, 671.

[48] G. Trejo, P. Ozil, E. Chainet, B. Nguyen, *J. Electrochem. Soc.* **1998**, *145*, 4090.

[49] B. Scharifker, G. Hills, *Electrochim. Acta* **1983**, *28*, 879.

[50] A. E. Alvarez, D. R. Salinas, *J. Electroanal. Chem.* **2004**, *566*, 393.

[51] S. Khorsand, K. Raeissi, M. A. Golozar, *J. Electrochem. Soc.* **2011**, *158*, D377.

[52] A. Radisic, J. G. Long, P. M. Hoffmann, P. C. Searson, *J. Electrochem. Soc.* **2001**, *148*, C41.

[53] X. Zhou, Y. Wang, Z. Liang, H. Jin, *Materials* **2018**, *11*, 1124.

[54] Z. Cao, P. Zhuang, X. Zhang, M. Ye, J. Shen, P. M. Ajayan, *Adv. Energy Mater.* **2020**, *10*, 2001599.

[55] Z. Hou, Y. Yu, W. Wang, X. Zhao, Q. Di, Q. Chen, W. Chen, Y. Liu, Z. Quan, *ACS Appl. Mater. Interfaces* **2019**, *11*, 8148.

[56] C. Wei, Y. Tao, H. Fei, Y. An, Y. Tian, J. Feng, Y. Qian, *Energy Storage Mater.* **2020**, *30*, 206.

[57] S. Park, H. J. Jin, Y. S. Yun, *Adv. Mater.* **2020**, *32*, e2002193.

[58] L. Ren, A. Wang, X. Zhang, G. Li, X. Liu, J. Luo, *Adv. Energy Mater.* **2019**, *10*, 1902932.